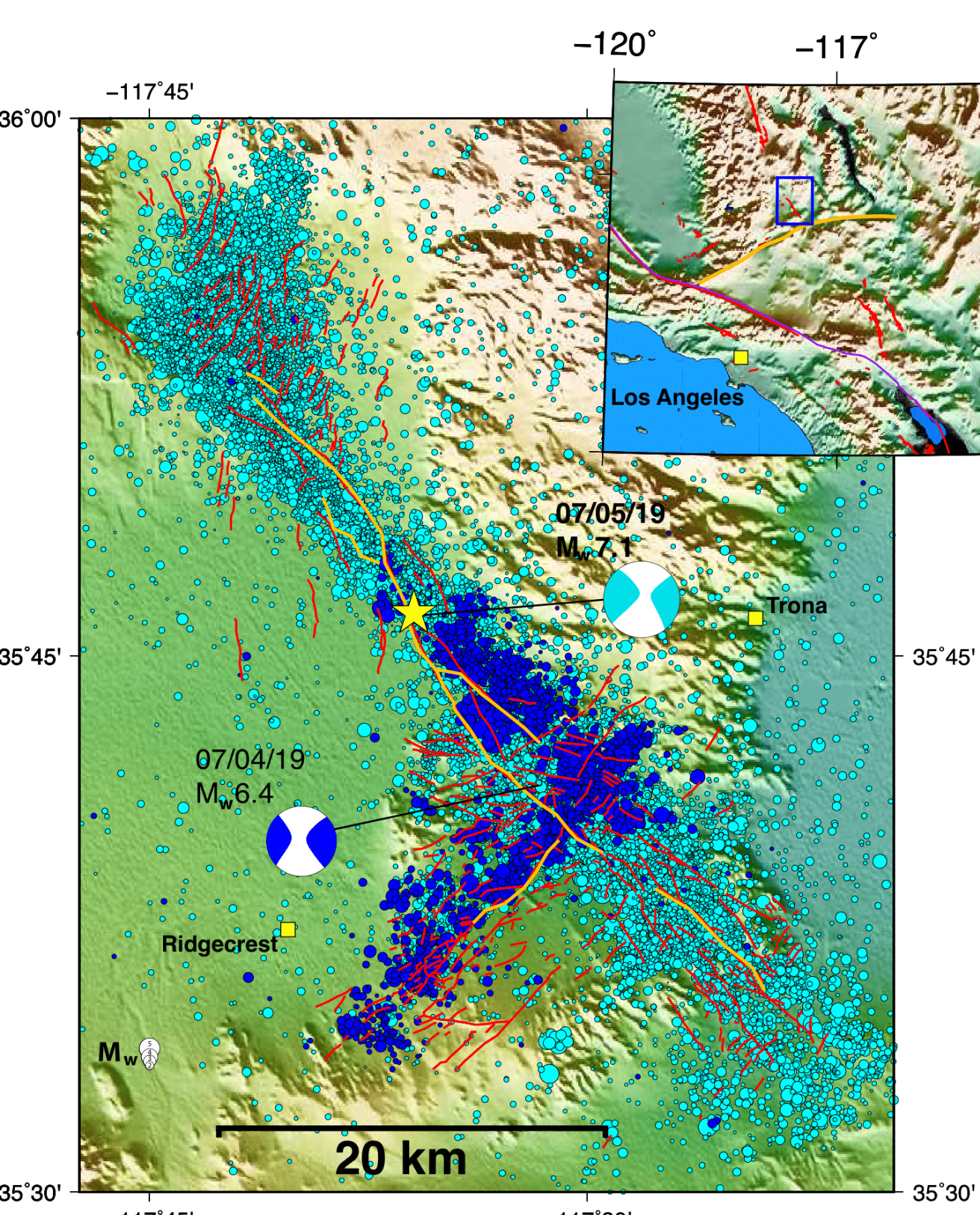


Introduction



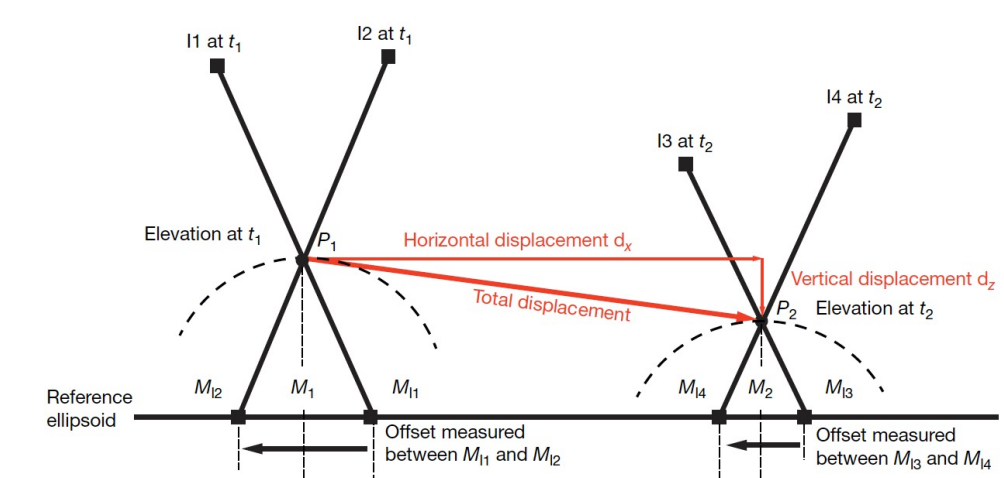
Above: Overview of the 2019 Ridgecrest earthquake sequence. The Mw 6.4 July foreshock focal mechanism is shown in dark blue with seismicity that occurred following this and before the Mw 7.1 mainshock on 5 July, 05:12 p.m. PST (shown as the cyan focal mechanism plots). Cyan circles show aftershocks following the mainshock event.

Research Questions:

- How variable are stresses along a rupture?
- Is the coseismic stress state similar to the orientation of the background stress or do dynamic stresses cause a significant deviation?
- Do more optimally orientated faults release larger coseismic slip?
- Could the degree of fault instability in relation to the stress field have favored the initiation location of the mainshock rupture?
- Does the fault orientation w.r.t the stress field affect the fault-zone rupture width and therefore rupture hazard?

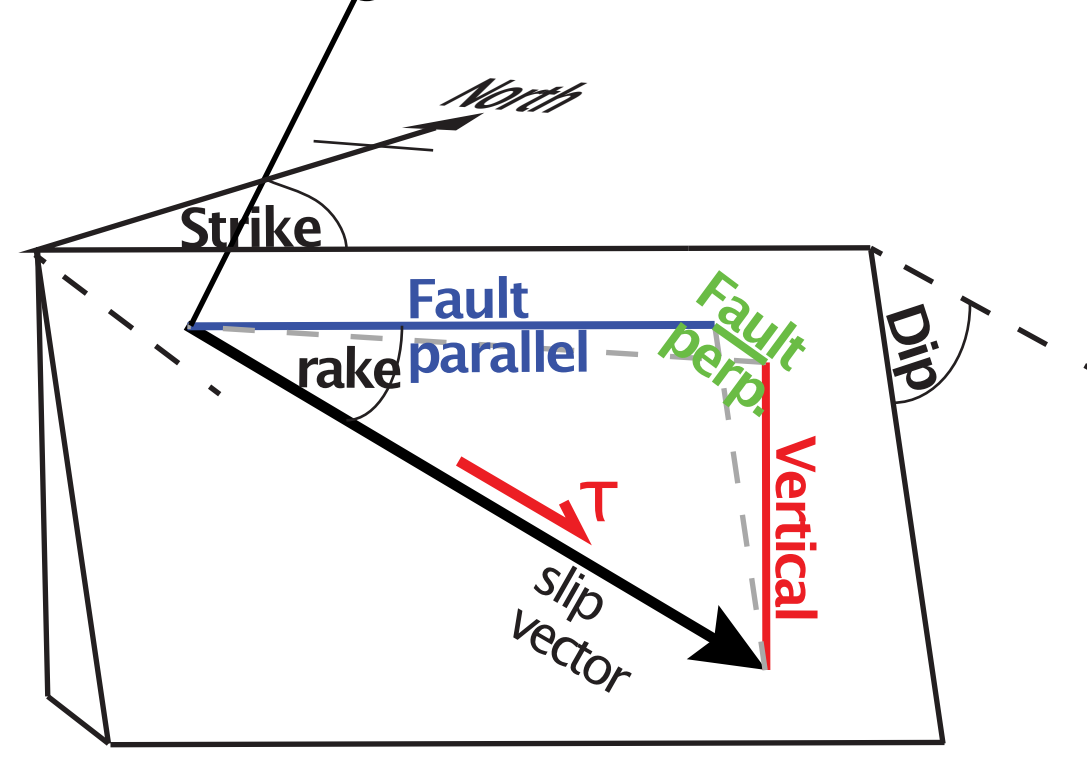
Methods

3D Optical Image Correlation



We have developed a new and automated optical image correlation method that can measure the full 3D surface deformation that can handle imagery from different sensors (World View 1, 2, 3 and SPOT-6 in this case) and different viewing geometries (i.e., not strict stereo-pairs).

3D slip vectors



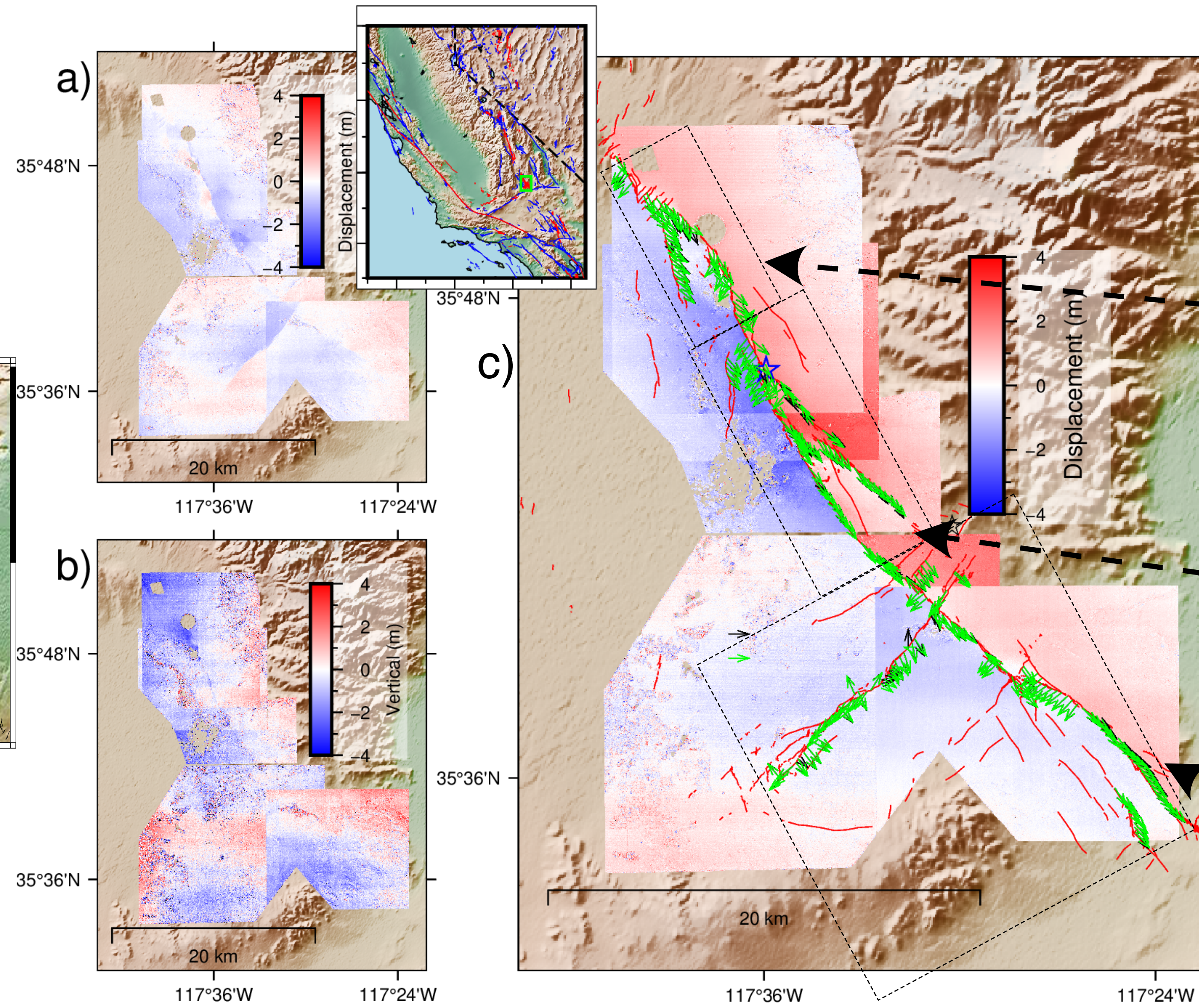
Schematic. From the 3D surface deformation maps we measure the **fault parallel**, **fault perpendicular** and **vertical** component of motion to reconstruct the full 3D coseismic slip vector every 138 meters along the rupture.

Stress Inversion

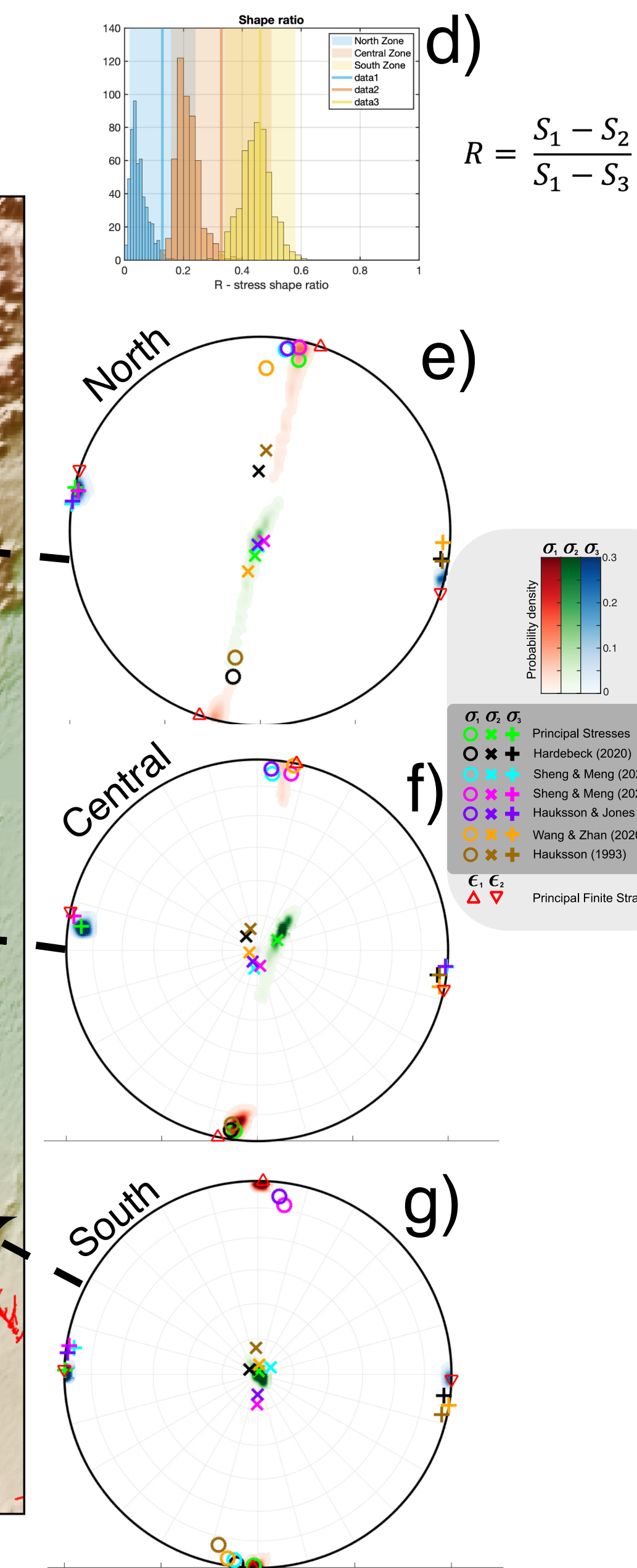
$$\mathbf{m} = (\mathbf{G}'\mathbf{G} + \mathbf{s}^2\mathbf{D}'\mathbf{D})^{-1}\mathbf{G}'\mathbf{d}$$

To estimate the coseismic stress orientation we invert the coseismic slip vectors ($n=240$) using an L1 iterative inversion scheme with a damping constraint to minimize spatial gradients between stress domains. Uncertainties are estimated via data random replacement bootstrapping.

3D Optical Displacement Maps and Stress results

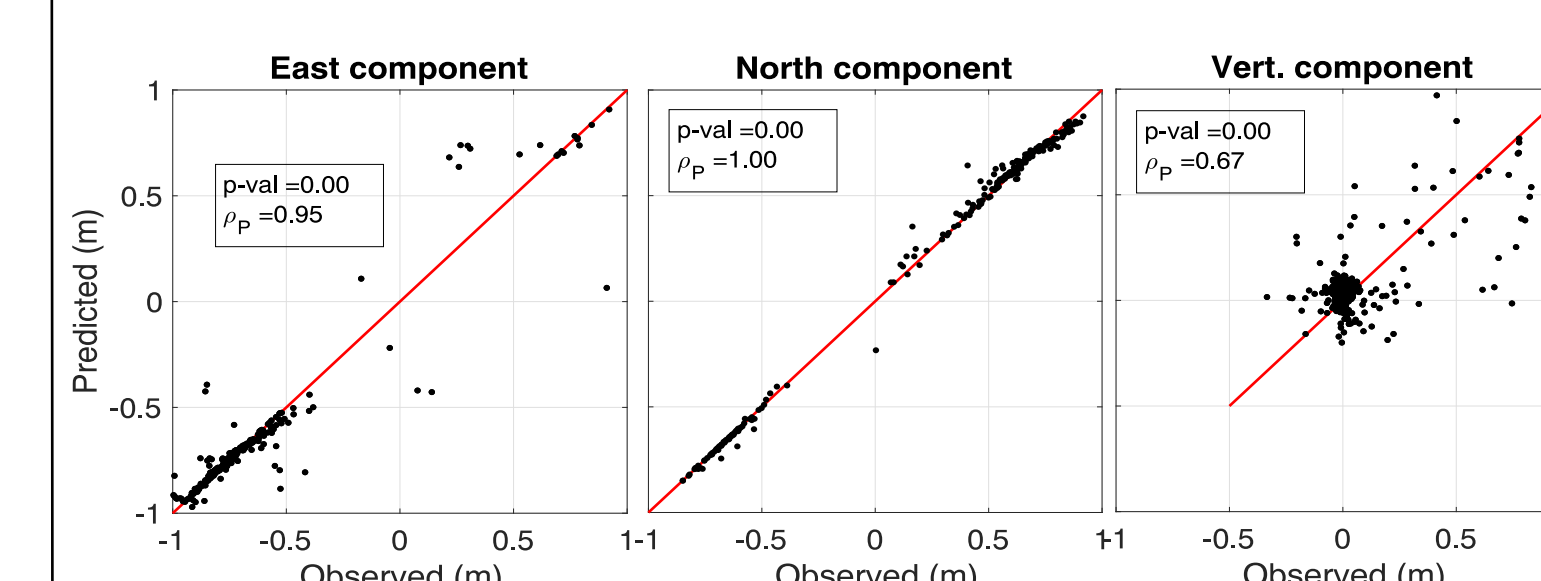


Above: a-c) 3D optical displacement maps. a) shows horizontal surface motion projected into the direction parallel to the foreshock (+ is NE, shown by the blue vector). b) shows vertical displacement. c) horizontal surface motion projected into the direction parallel to the mainshock (+ is SE, shown by the blue vector). Black vectors show the observed slip vectors, while green show the predictions from our best fitting stress model.

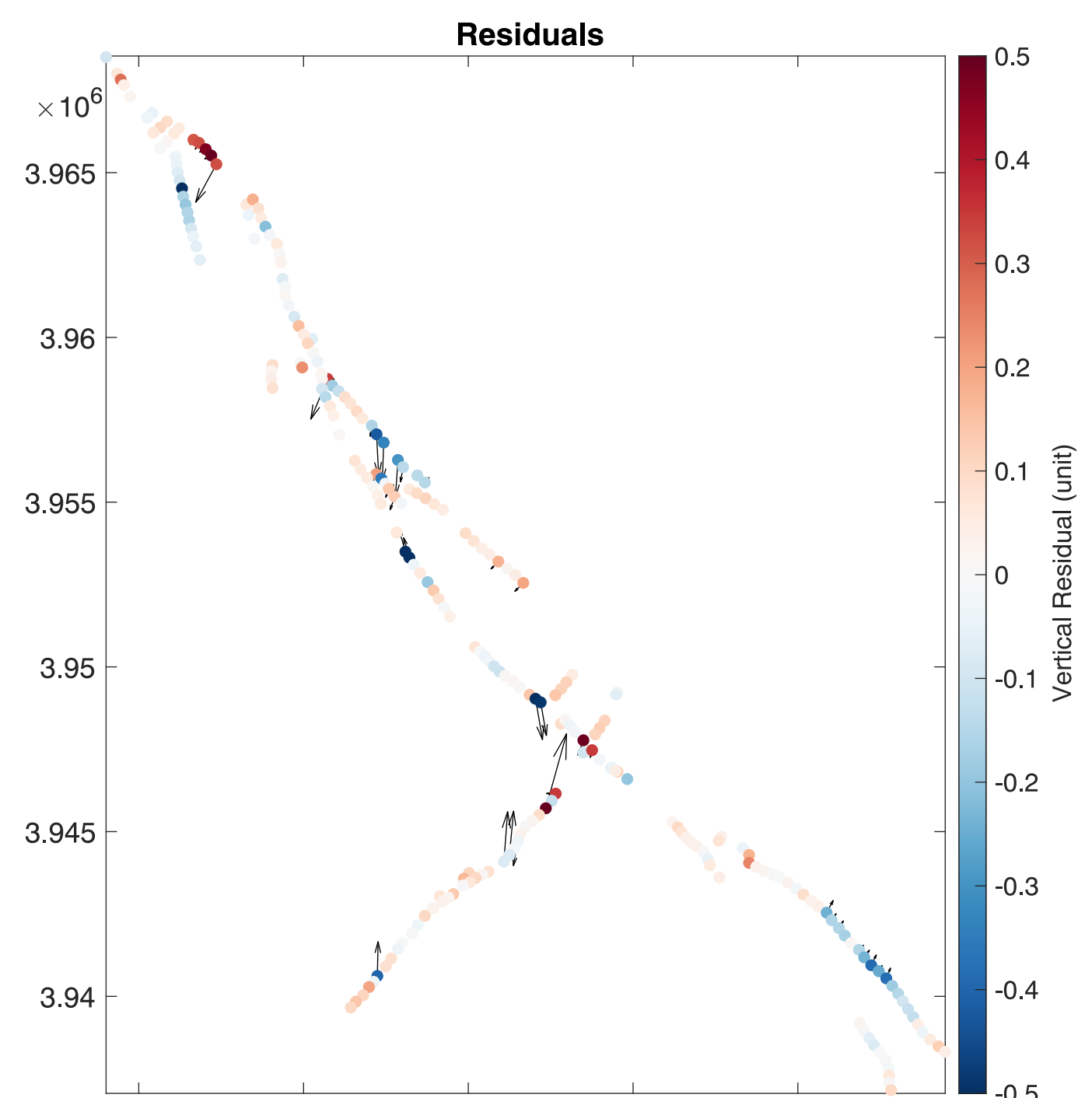


Above: d-g) shows the stress orientation results inverted from the slip vectors projected in lower hemisphere and separated for the 3 stress zones. d) shows the stress ratio (R) where lower values indicate more transensional and higher values transensional stress regimes. (e-g) We find a northeastward rotation of the stress orientation by 15 degrees from south to north along the mainshock rupture. Our stress orientations are in strong agreement with estimates of the background (pre-Ridgecrest) stress state from 4 previously published studies (colored symbols).

Model Misfits

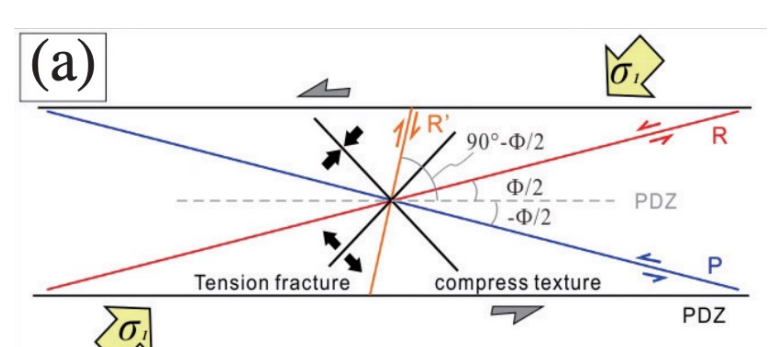


Above: Assessment of stress model fit by comparing the observed vs predicted slip in the east (left), north (middle) and vertical (right) components. Overall we find an excellent fit with 94% Percent of variance reduction for both the mainshock and foreshock with a 3 zone stress model. The vertical direction has the poorest fit, largely because most slip vectors had lateral strike slip motion so there is little signal and the vertical displacement maps are less well constrained than the horizontal because of the high degree of collinearity of the satellite look vectors.



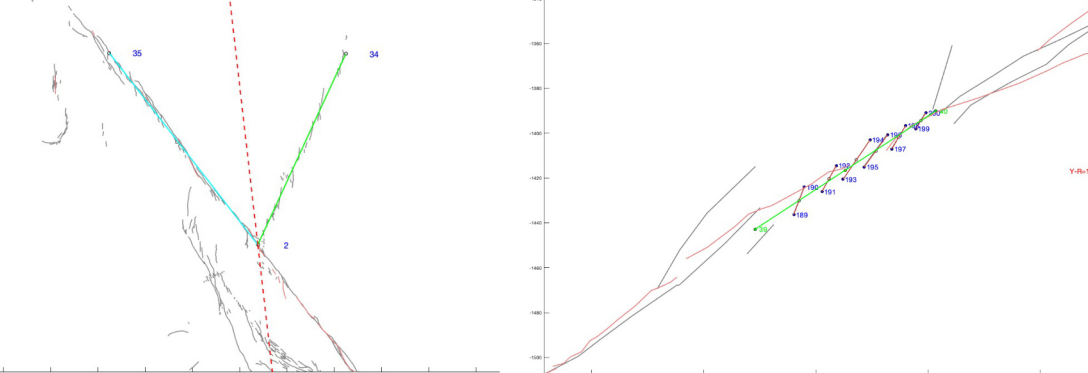
Above: Map view of the residuals of the unit slip vectors with horizontal components shown as vectors and vertical component as colored.

Stress Model Validation



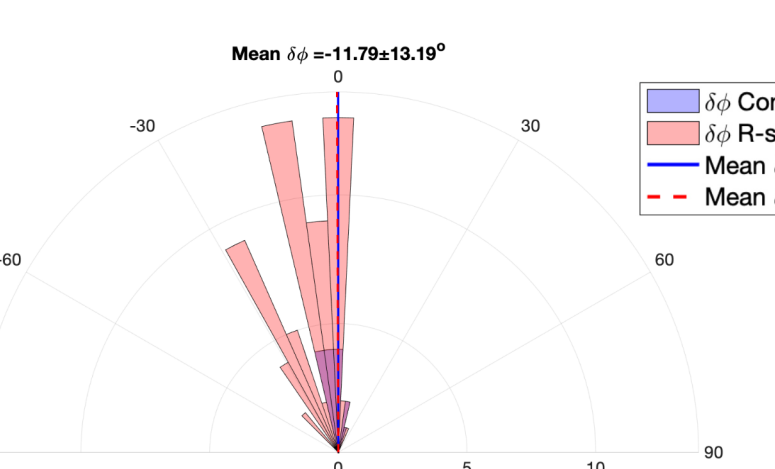
Left: Illustration of the relation of maximum compressive stress to the orientations of fractures. Here we use this relation to estimate the azimuth of SHmax from mapping and measuring half the dihedral angle between 295 coseismic Riedel (R-shear), through-going (Y-shear) and conjugate-Riedel fractures (R').

Mapping Riedel fractures → SHmax

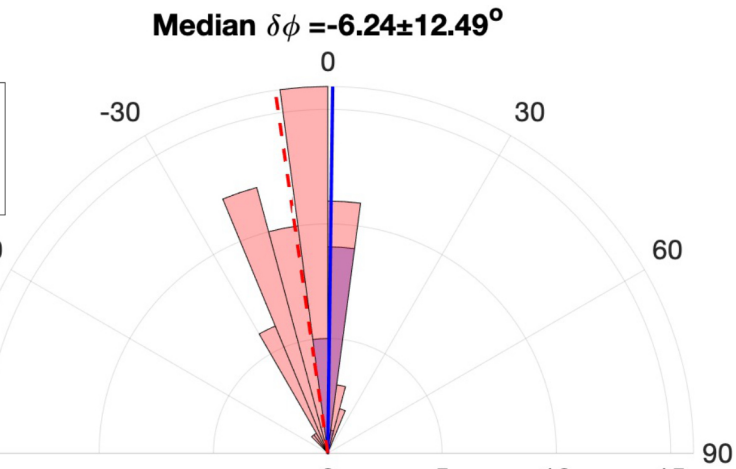


Left: Examples of mapped R-R' fractures (leftmost) and R-Y fractures (right). The dashed red line in left figure shows the azimuth of SHmax.

SHmax angular difference for 1 zone stress model

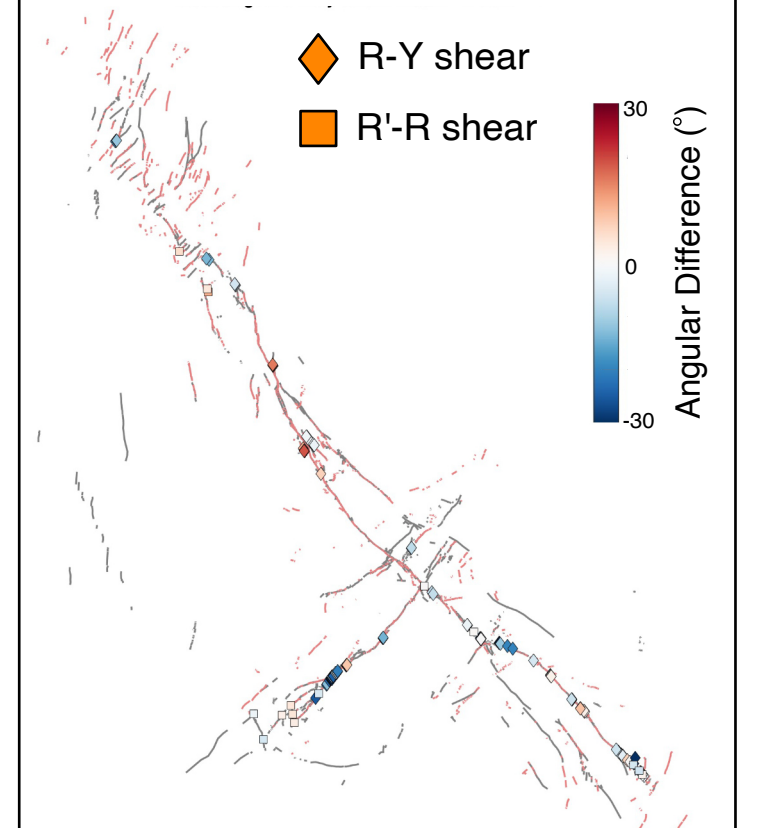


SHmax angular difference for 3 zone stress model



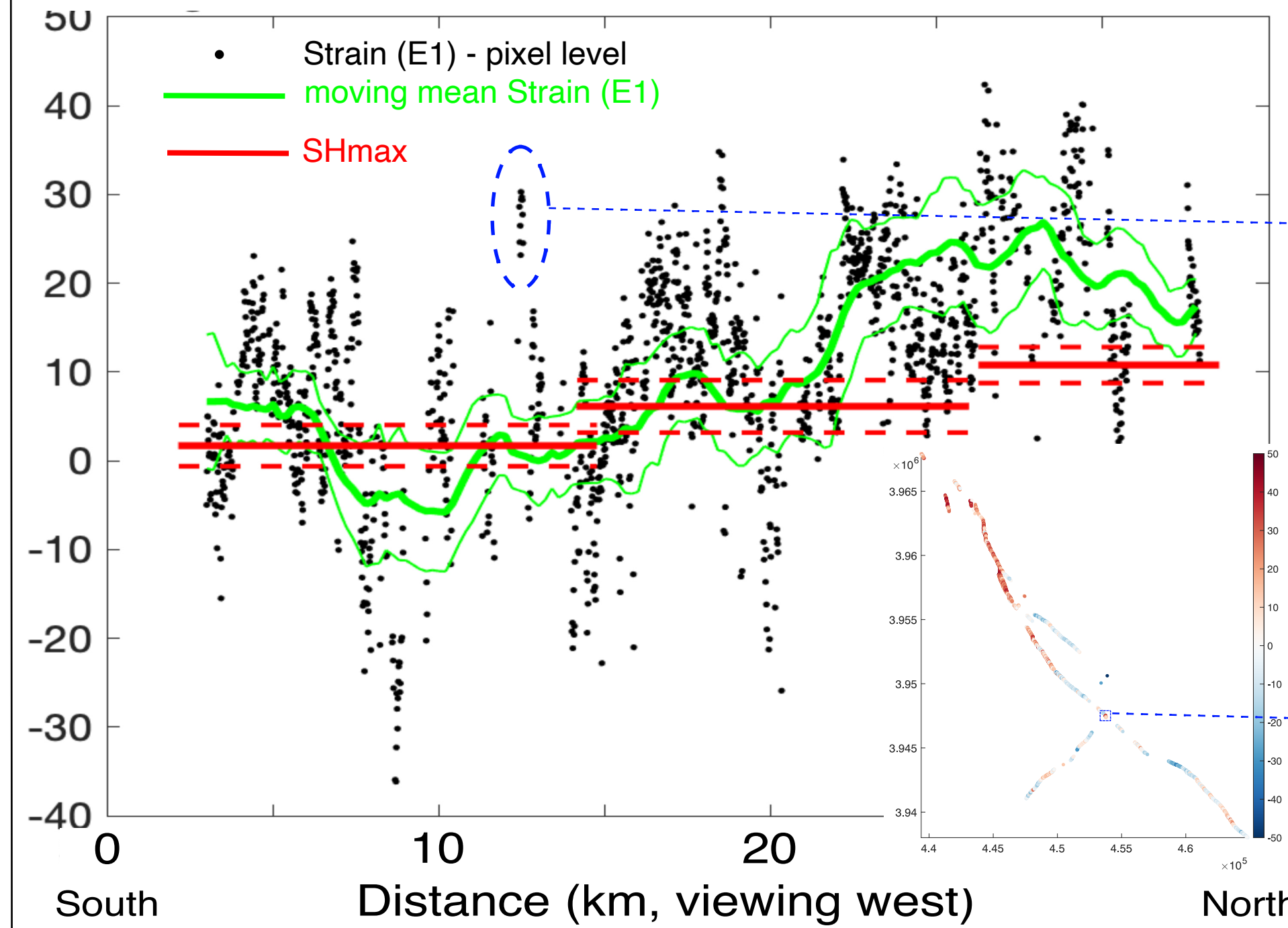
Above: Polar histograms showing the angular difference between the SHmax inferred from coseismic fracture orientations to our modeled SHmax estimate (following Lund and Townend, 2007). Left shows the angular difference for the uniform stress model (1 zone). Right shows the median angular difference is 6.23 with sample 1 of 12.5. We note that using a 2 zone stress model over a uniform one decreases the misfit by 50%, a 3 zone model shows no significant increase from 2 zones.

Map of SHmax misfit

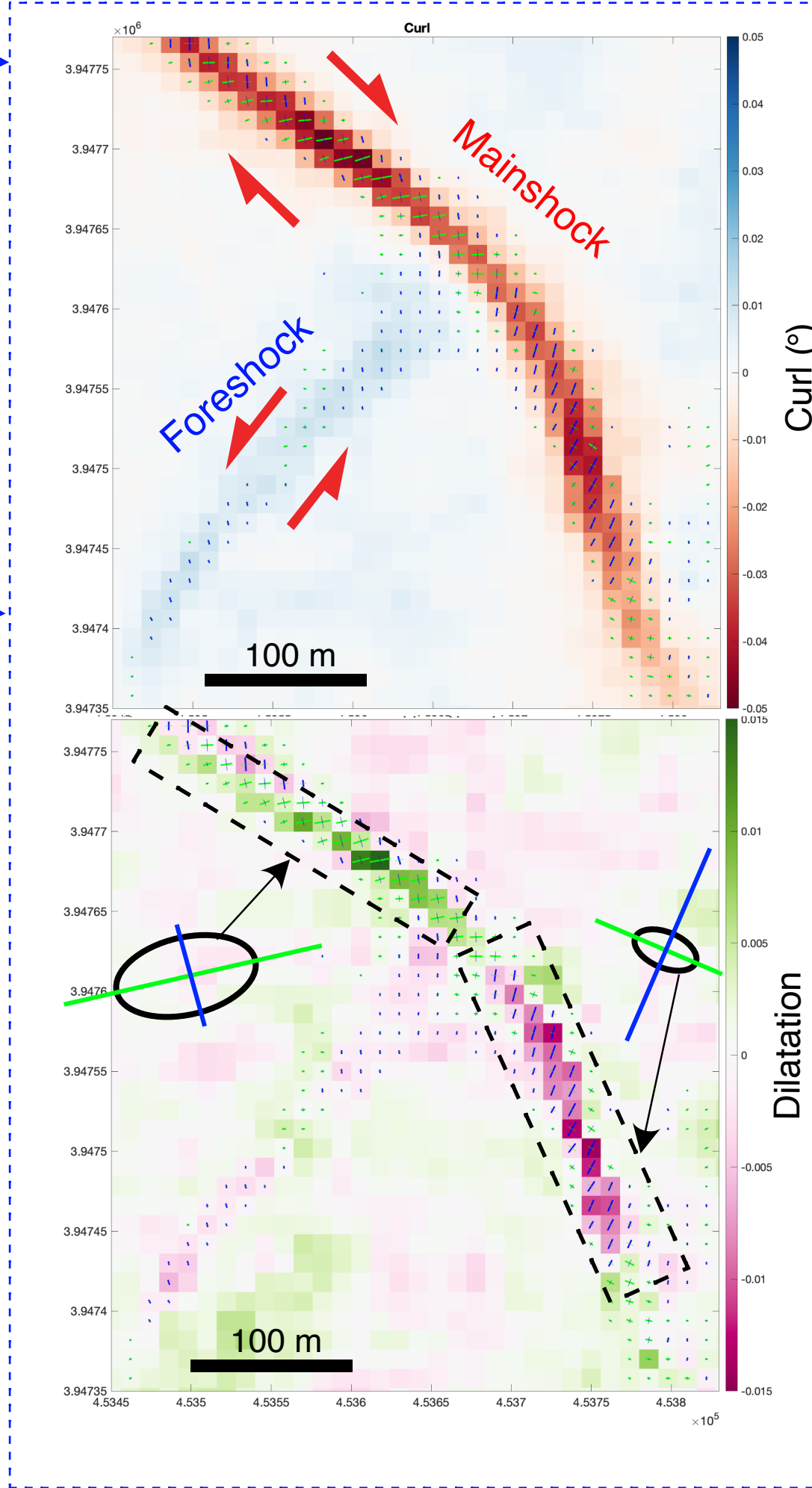


Above: Map view of the location of the R-Y and R-R' fractures with colors showing the angular difference between the measured SHmax and that from our stress inversion

Stress vs Finite Strains



Below shows the curl (top) and dilatational finite strain (bottom) at the intersection of the foreshock and mainshock ruptures. Both the trend of the principal finite strains and sign of dilatation (highlighted by box) changes along the mainshock rupture, across the intersection. This suggests further evidence that directions of strain are affected by stresses, which are local in this case due to rupture of the foreshock altering the local stress state



$$\text{Displacement gradients } (\Delta u_i) \quad \frac{\Delta u_x(i,j)}{\Delta x} = \frac{u_x(i+1,j) - u_x(i-1,j)}{2\Delta x}$$

$$\text{Finite Strain Tensor (E)} \quad \mathbf{E} = \begin{bmatrix} E_{xx} & E_{xy} \\ E_{yx} & E_{yy} \end{bmatrix}$$

$$E_{ij} = \frac{1}{2} \left(\frac{\Delta u_i}{\Delta x_j} + \frac{\Delta u_j}{\Delta x_i} + \frac{\Delta u_k \Delta u_k}{\Delta x_i \Delta x_j} \right)$$

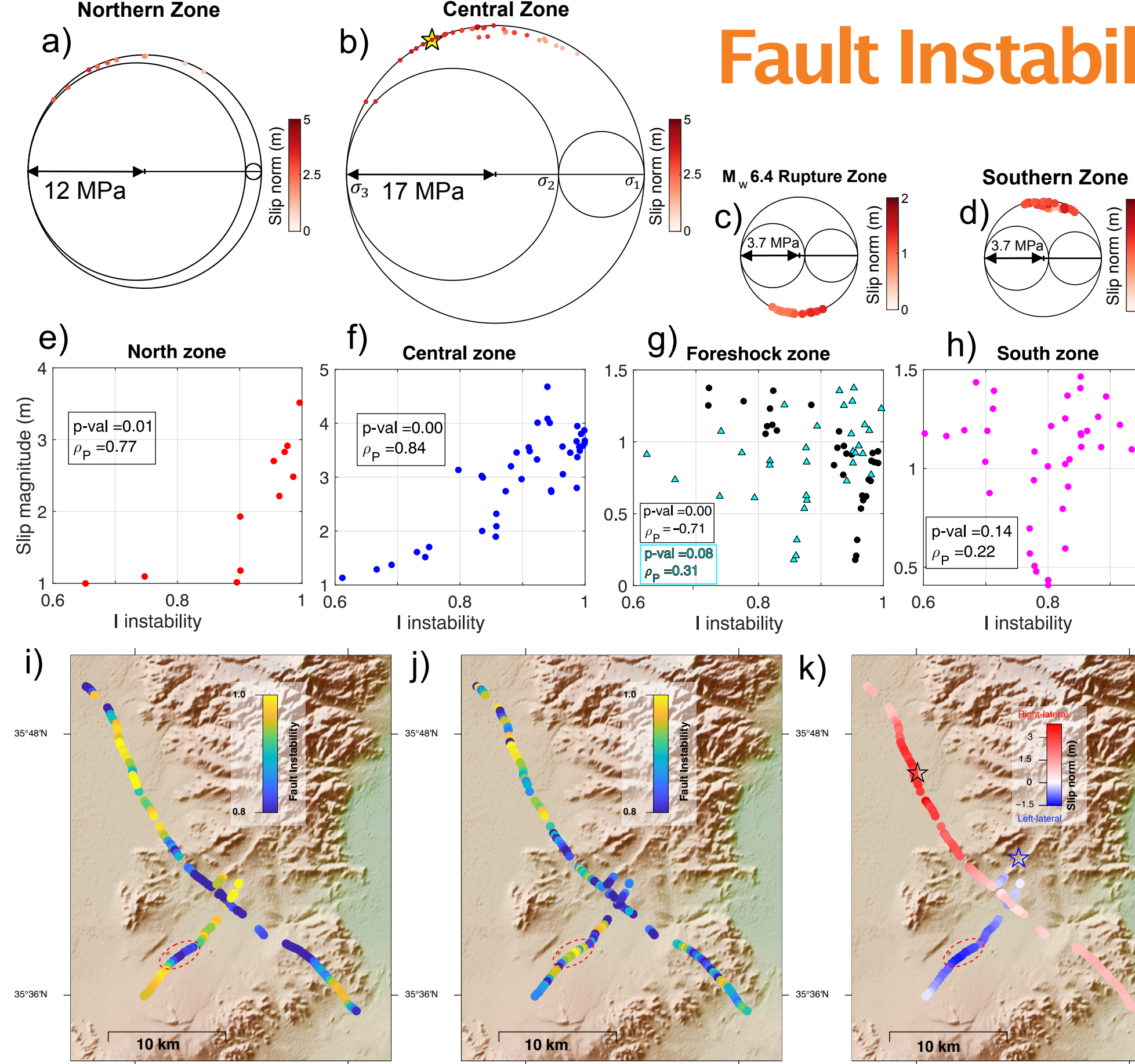
$$\text{Curl (c)} \quad \omega = \frac{c}{2} = \frac{1}{2} \left(\frac{\Delta u_x}{\Delta y} - \frac{\Delta u_y}{\Delta x} \right)$$

Above, top: Shows that similar to the rotation of SHmax from our stress model (red lines) the trend of the coseismic finite principal strain directions (black dots, with moving average shown in green) also rotates as a function of distance from south to north along the mainshock. Inset map also illustrates how trend of E-1 finite principal contractional direction rotates along-strike. One can see shorter scale variations of stress orientation.

Above, middle: polar histograms of E-1 (blue regions) for each of the 3 stress zones compared to SHmax (red lines).

Above, bottom: Zoom in plot illustrating the rotation of the principal finite E-1 direction in the 3 different zones

Fault Instability

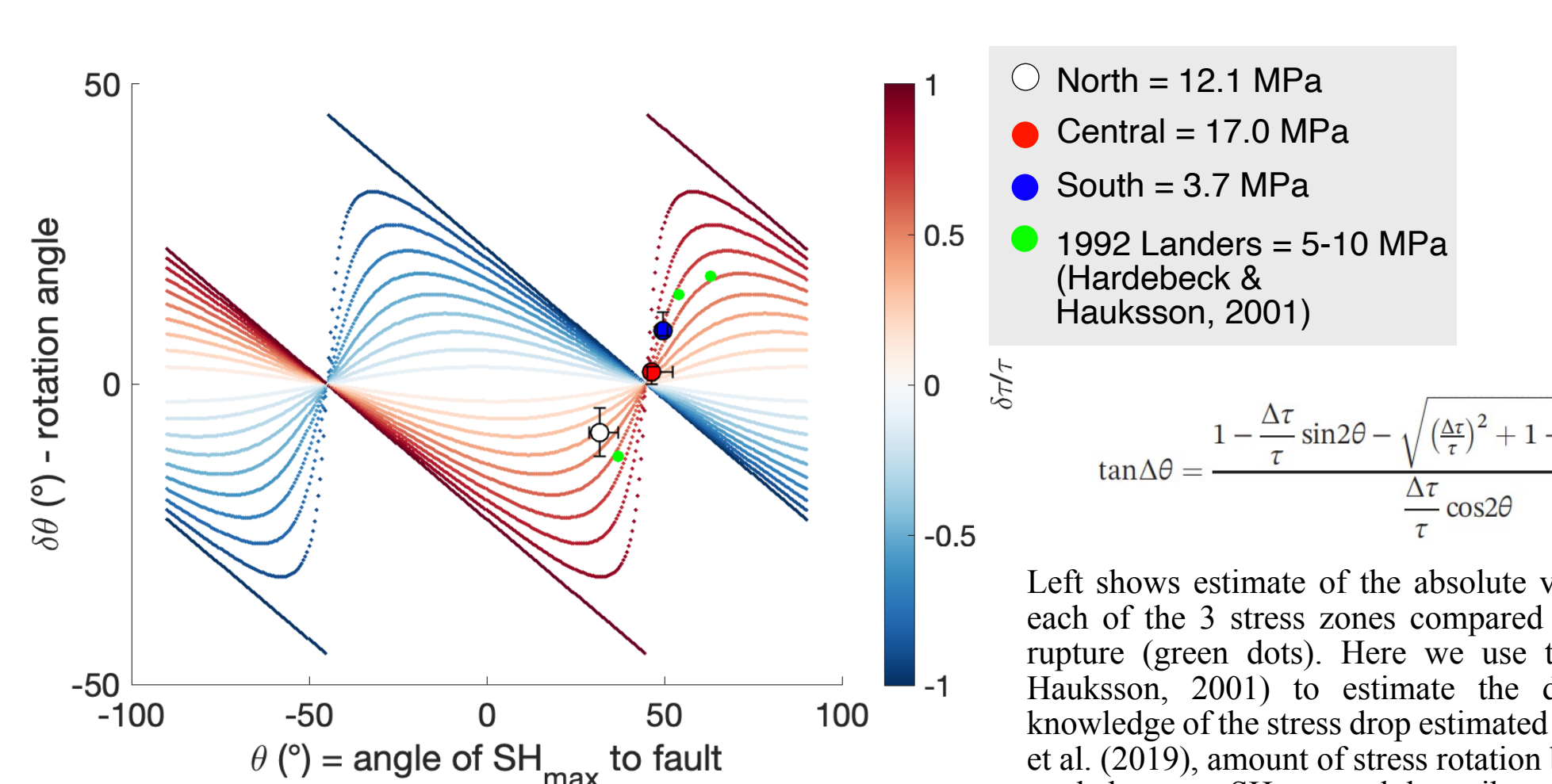


Top row (a-d) shows Mohr circles from our stress model with colors denoting the magnitude of coseismic slip.

Middle row (e-h) shows the coseismic slip magnitude vs fault instability (assuming $\mu=0.6$). g) black dots shows fault instability values estimated from regional stress model with unexpected strong negative correlation, while cyan triangles show fault instability estimated using E-1 as a proxy for SHmax to account for local stress rotations, showing an improved correlation.

Bottom row (i-k): Map view of the fault instability, which we find is largest at the site of the hypocenter, suggesting the faults in this region were critically stressed. j) shows fault instability re-estimated assuming E-1 is parallel to SHmax to account for local rotations of stress not resolved by our regional model

Deviatoric Stresses



Left shows estimate of the absolute value of the deviatoric stresses for each of the 3 stress zones compared to estimates of the 1992 Landers rupture (green dots). Here we use the equation from (Hardebeck & Hauksson, 2001) to estimate the deviatoric stress magnitude with knowledge of the stress drop estimated from finite fault slip model of Ross et al. (2019), amount of stress rotation before and after the mainshock and angle between SHmax and the strike of coseismic rupture.

Summary

- We solved for the full 3D surface deformation pattern of the 2019 Ridgecrest earthquake sequence using a newly developed multi-sensor, multi-viewing optical image correlation method.
- How variable are stresses along a rupture?
 - From inverting the 3D coseismic slip vectors we find a 15° rotation of the coseismic stress state from south-to-north along the mainshock rupture.
- We also find a similar 15° rotation of the finite principal strains along strike and smaller scale variability of strain suggesting stresses likely rotate at fault intersections, stopovers and terminations.
- Is the coseismic stress state similar to the orientation of the background stress or do dynamic stresses cause a significant deviation?
 - Our coseismic stresses are in strong agreement with the background stresses estimated from inverting local mechanisms, suggesting no observable rotation caused by the dynamic stresses (which is expected to rotate slip vectors).
- Do more optimally orientated faults release larger coseismic slip?
 - We find evidence in 2 out of the 3 stress zones of for strong evidence of higher slip where faults have more of an optimal alignment to the background stress field.
- Could the degree of fault instability in relation to the stress field have favored the initiation location of the mainshock rupture?
 - From estimating the fault instability criterion we find it is highest at the location of the mainshock epicenter.
- Does the fault orientation w.r.t the stress field affect the fault-zone rupture width and therefore rupture hazard?
 - This is on-going work, but we aim to compare the fault zone width from the strain maps to the coseismic stress orientation estimate.

References

Ross, Z.E., Ishii, B., Jia, Z., Stephenson, O.L., Zhong, M., Wang, X., Zhan, Z., Simons, M., Fielding, E.J., Yun, S.H. and Hauksson, E., 2019. Hierarchical interlocked orthogonal faulting in the 2019 Ridgecrest earthquake sequence. *Geophysical Research Letters*, 46(10), pp. 11571-11582.

Michael, A.J., 1984. Determination of stress from slip data: faults and folds. *Journal of Geophysical Research*, 89(10), pp. 11571-11582.

Hardebeck, J.L. and Hauksson, E., 2001. Crustal stress field in southern California and its implications for fault mechanics. *Journal of Geophysical Research*, 106(B10), pp. 21859-21862.

Sheng, S. and Meng, L., 2002. Stress field variation during the 2019 Ridgecrest earthquake sequence. *Geophysical Research Letters*, 29(15), p. 2002GL015722.

Hardebeck, J.L., 2000. A Stress-Similarity Triggering Model for Aftershocks of the Mw 6.4 and 7.1 Ridgecrest Earthquakes. *Bulletin of the Seismological Society of America*, 71(04), pp. 1716-1727.

Lund, B. and Townend, J., 2007. Calculating horizontal stress orientations with full or partial knowledge of the tectonic stress tensor. *Geophysical Journal International*, 170(3), pp. 1326-1335.

Wang, X. and Zhan, Z., 2020. Geomechanics and fault geometries of the 2019 Ridgecrest sequence: Insight from aftershock moment tensor catalog using 3-D Green's functions. *Journal of Geophysical Research*, 125(5), p. 2020JB019577.

Acknowledgements

This work was funded by a NASA ROSES Earth Surface and Interior focus area grant to Chris Milliner (co-PI) and Jean-Philippe Avouac (PI) and SCEC grant #19222.